GPI 2.0: Pre-integrated pyramid wavefront sensor results

Saavidra Perera[a], Jérôme Maire[a], Clarissa R. Do Ó[a], Jayke S. Nguyen[a], Vincent Chambouleyron[b], Quinn M. Konopacky[a], Jeffrey Chilcote[c], Brian Sands[c], Randall Hamper[c], Matthew Engstrom[c], Joeleff Fitzsimmons[d], Dan Kerley[d], Bruce Macintosh[b], Christian Marois[d], Fredrik Rantakyrö[e], Dmitry Savranksy[f], Jean-Pierre Veran[d], Guido Agapito[g], S. Mark Ammons[h], Marco Bonaglia[g], Marc-Andre Boucher[i], Joel Burke[c], Daren Dillon[b], Jennifer Dunn[d], Simone Esposito[g], Guillaume Filion[i], Oyku Galvan[j], Jean Thomas Landry[i], Olivier Lardiere[d], Duan Li[f], Alex Madurowicz[b], Teo Mocnik[j], Dillon Peng[c], Lisa Poyneer[h], Carlos Quiroz[e], Garima Singh[j], and Eckhart Spalding[k]

[a]Department of Astronomy and Astrophysics, University of California San Diego, La Jolla, CA 92093, USA
[b]University of California Santa Cruz, Santa Cruz, CA 95064, USA
[c]Department of Physics, University of Notre Dame, 225 Nieuwland Science Hall, Notre Dame, IN 46556, USA
[d]National Research Council of Canada Herzberg, 5071 West Saanich Rd, Victoria, BC, V9E 2E7, Canada
[e]Gemini Observatory/NSF NOIRLab, Casilla 603, La Serena, Chile
[f]Sibley School of Mechanical and Aerospace Engineering, Cornell University, Ithaca, NY 14853, USA
[g]Arcetri, Largo Enrico Fermi 5, I - 50125 Florence, Italy
[h]Lawrence Livermore National Laboratory, Livermore, CA 94551, USA
[i]OMP inc., 146 Bigaouette St. Quebec City, QC, Canada, G1K 4L2
[j]Gemini Observatory/NSF NOIRLab, 670 N. A'ohoku Place, Hilo, Hawai'i, 96720, USA
[k]University of Sydney, Camperdown, NSW 2050, Australia

ABSTRACT

The Gemini Planet Imager (GPI) is a high-contrast imaging instrument designed to directly detect and characterise young, Jupiter-mass exoplanets. After six years of operation at the Gemini South Telescope in Chile, the instrument is being upgraded and moved to the Gemini North Telescope in Hawaii as GPI 2.0. Several improvements have been made to the adaptive optics (AO) system as part of this upgrade. This includes replacing the current Shack-Hartmann wavefront sensor with a pyramid wavefront sensor (PWFS) and a custom EMCCD. These changes will increase GPI's sky coverage by accessing fainter targets, improving corrections on fainter stars and allowing faster and ultra-low latency operations on brighter targets. The PWFS subsystem was independently built and tested to verify its performance before being integrated into the GPI 2.0 instrument. This paper will present the pre-integration performance test results, including pupil image quality, throughput and linearity without modulation.

Keywords: Adaptive Optics, Pyramid Wavefront Sensor, Wavefront Sensing, Gemini Planet Imager, High-Contrast Imaging

Further author information: (Send correspondence to Saavidra Perera)
Saavidra Perera: E-mail: sperera@ucsd.edu

Adaptive Optics Systems IX, edited by Kathryn J. Jackson, Dirk Schmidt, Elise Vernet,
Proc. of SPIE Vol. 13097, 130971S · © 2024 SPIE · 0277-786X
doi: 10.1117/12.3020360

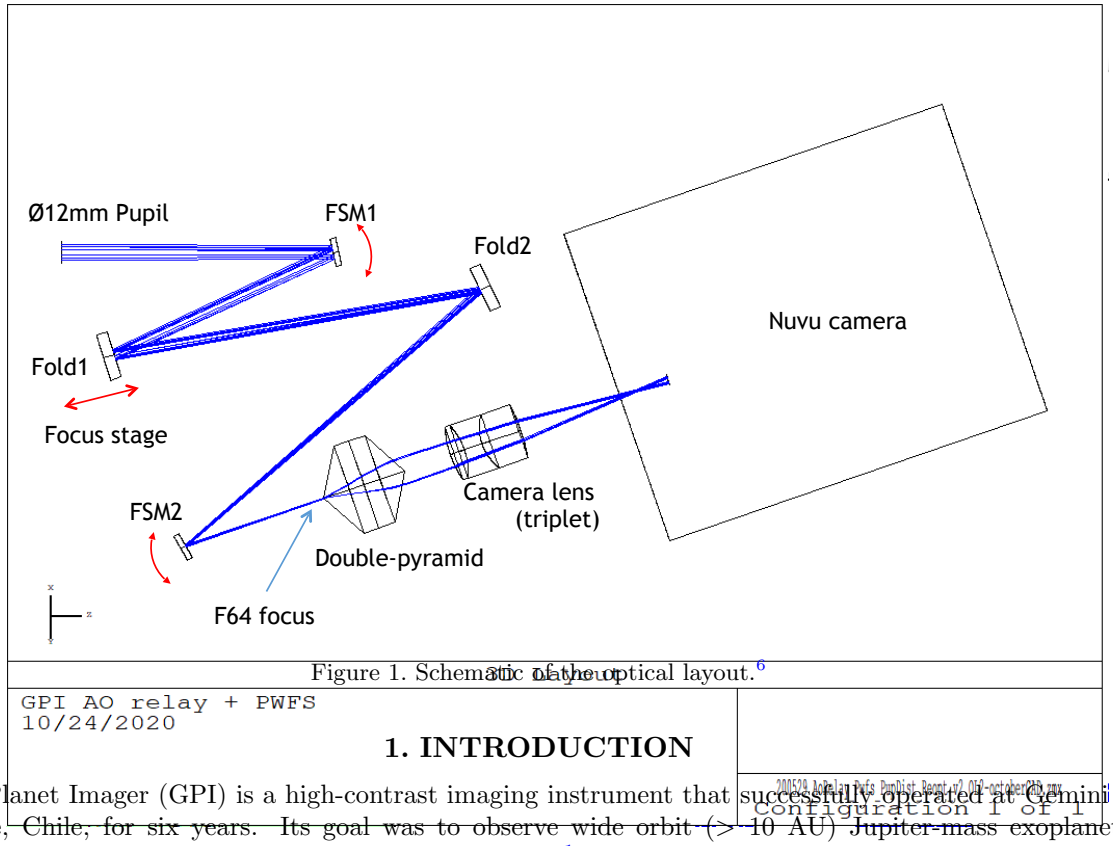

Figure 1. Schematic of the optical layout.[6]

1. INTRODUCTION

Gemini Planet Imager (GPI) is a high-contrast imaging instrument that successfully operated at Gemini South Telescope, Chile, for six years. Its goal was to observe wide orbit (> 10 AU) Jupiter-mass exoplanets and resolve circumstellar material around young, nearby stars.[1] In August 2020 it was decommissioned to be moved to Gemini North Telescope, Hawaii USA. This presented an opportunity to envisage new scientific goals and assess the required upgrades to become GPI 2.0. These new goals, outlined in full in Chilcote et al. (2020),[2] require GPI 2.0 to be more sensitive to fainter planets and to reach deeper contrasts at smaller inner working angles. Therefore, upgrades to the adaptive optics (AO) system, coronagraphic masks, calibration unit (CAL) and integral field spectrograph (IFS) are taking place.[3] The main upgrades to the AO system include:

- Replacing the current Shack-Hartmann wavefront sensor with a pyramid WFS (PWFS)
- Replacing the current CCD with a custom Nüvü EMCCD
- Updating the current real-time controller (RTC) software to the Herzberg Extensible Adaptive Real-time Toolkit (HEART)[4]

The subject of this paper is the PWFS, which will enable access to fainter WFS targets (I band magnitude of 14) whilst also providing more stable operations on brighter targets. GPI 2.0's PWFS has benefited from the research and design of the Thirty Meter Telescope (TMT) Narrow Field InfraRed Adaptive Optics System (NFIRAOS),[5] using many of the same components. The PWFS was built, aligned and tested at UC San Diego before its integration into the GPI 2.0 instrument at the University of Notre Dame in May 2024. In this paper pre-integration tests as well as the status of the integration will be presented.

2. PWFS SUBSYSTEM DESIGN & BUILD

2.1 Design

A complete description of the PWFS design, including the opto-mechanical design, is presented in Fitzsimmons et al. (2020).[6] Figure 1 shows the ray trace of the PWFS, which has a 12 mm diameter pupil and an f/64 beam reflected from the GPI science beamsplitter dichroic with a cut-off wavelength of 925 nm. The PWFS employs key components as described below:

- Two fast steering mirrors (FSM). FSM1 will modulate and dither the focused spot around the tip of the pyramid. The typical radius of the modulation circle, produced by FSM1, will be $3\lambda/D$.
- Two fold mirrors (Fold), where Fold1 is mounted on a transitional stage for focus capabilities.
- Four-sided double-pyramid, splitting the light into four channels. It is comprised of two different class materials combined along their base, and is identical to that used by NFIRAOS.
- A triplet (camera) lens to image the pupils onto the EMCCD.
- An EMCCD with near-zero noise, high quantum efficiency and fast readout. It will operate at frequencies up to 2 kHz (though capable of 3 kHz).
- Anodised aluminium bench, with a hollowed frame to reduce the mass of the PWFS.
- Baffle and field stop to reduce background noise and source confusion.

It is important to note that the pupil plane is not at FSM1 (as shown in Figure 1), which means for large modulations the image on the EMCCD will move, resulting in smearing. This is further discussed in section 3.1

2.2 Build

The PWFS was built and aligned at UC San Diego in a class 1000 cleanroom, before being shipped to the University of Notre Dame for its integration. The manufacturers of each component are listed in table 1.

Component	**Manufacturer**
EMCCD	Nüvü Camera
Stages	Physik Instrumente
Mirrors	Coastline Optics
Camera lens	BVM Optical Technologies
Double four-sided pyramid	BVM Optical Technologies
PWFS bench & optomechanical components	Opto-Mécanique de Précision (OMP)

Table 1. List of the PWFS components and manufacturers used.

A key component of the PWFS is the EMCCD which will enable observations of fainter targets and measure the atmosphere at a faster frequency (moving from 1 kHz to 2 kHz). It uses the Teledyne e2v CCD220 8 outputs for a faster readout, giving a 240 pixels $\times$ 240 pixels area, where the pixel length is 24μm. During the build of the PWFS it was found that the Nüvü camera suffered from charge diffusion resulting in blurry images as described in Do Ó et al. (2024).[7] This was due to the inverted readout mode set by Nüvü, which was subsequently changed to non-inverted readout mode. This mode change increased the dark current. However, for the short exposures we are using this will have a negligible impact on our results.

The PWFS was initially aligned using a test source unit (TSU) with a 625 nm laser to mimic the f/64 beam of the telescope. With the TSU the pupil image quality was initially assessed (for a full breakdown of the tests performed see Perera et al. (2022)[8]). The throughput was measured as 98 %. Based on the requirement of the individual components the transmission should be 95%. In April the PWFS was shipped to the University of Notre Dame to be integrated into GPI. Section 3 presents the pre-integration tests performed pre- and post-shipping to assess pupil image quality. The results remained unchanged. In May it was integrated into the GPI instrument, see figure 2.

3. PUPIL IMAGE QUALITY

3.1 Focus

To image the correct pupil plane, a resolution card was placed at the pupil stop located inside the TSU. This was found by changing the position of the camera lens through positive to negative defocus. The camera lens lies inside a tube with external threads to mount to the holder, allowing the position of the lens to move towards and away from the EMCCD. At the correct plane, the pupil separation was expected to be 120 pixels (the requirement 120 pixels). The measured separation between each horizontal and vertical pair was between 122 and 124 pixels. Since FSM1 is not located at the pupil plane, large modulations will result in movement of the pupil positions. For a modulation radius of $20\lambda/D$, the expected movement is ~ 1 pixel, which is what we measured. This further confirms the focus of the correct plane. For $10\lambda/D$ this movement is ~ 0.5 pixels. Given that the typical modulation radius will be $3\lambda/D$, this smearing will be negligible. Figure 3 shows the final pre-integrated non-modulated and modulated images of the pupils. It can be seen there are edge effects between the EMCCD outputs (most prominent between the top two left outputs, seen as a vertical line through the pupil) that are not removed in the bias or the flats. This requires further investigation.

To ensure there was no lateral shift of the pupils with wavelength, the fibre-fed TSU was replaced with 850 nm wavelength. No change in pupil position was measured.

3.2 Pupil Image Distortion

The measurements described below were based on the TMT NFIRAOS test plan. The pupil images are assessed by pupil radius (Equation 1), pupil differential distortion (Equation 2) and RMS common distortion (Equation 3). These parameters were calculated by finding the central position of each pupil, and then converting to polar coordinates (see Figure 4), before interpolating and thresholding.

(i) Pupil radius is defined as

$$R_X = \overline{X_i} \ , \tag{1}$$

where denotes the pupil image A, B, C or D and i is the number of radius measurements as shown in Figure 5. The expected radius was 30 ± 0.5 pixels i.e 720 ± 12 μm. All four pupils were measured to be within 0.4 pixels of the 30 pixels radii.

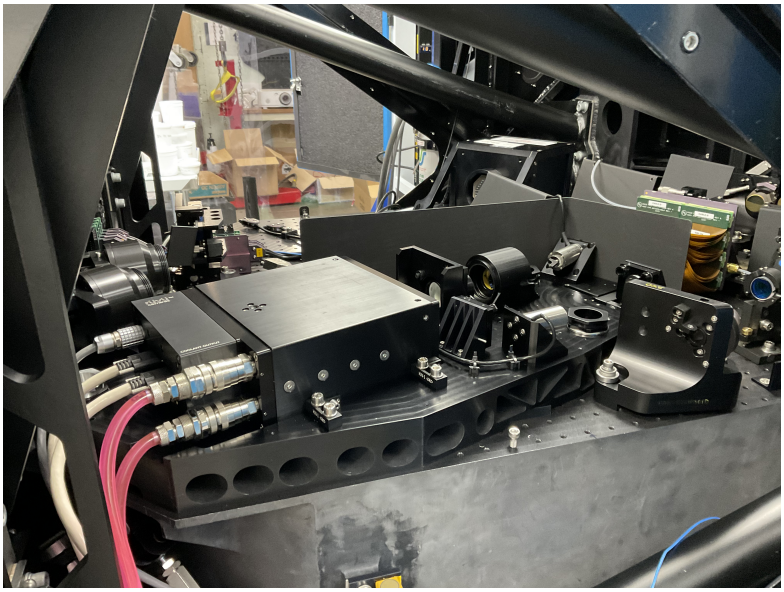

Figure 2. The PWFS integrated and mounted onto the GPI bench.

(ii) Pupil differential distortion between each pupil image combination:

$$D_{A-B} = Max(|A_1 - B_1|, |A_i - B_i|, ...) \ . \tag{2}$$

The maximum differential distortion was between pupils B and D with a value of 0.49 pixels. The minimum with C and D with a value of 0.27 pixels. The requirement was 0.33 pixels (8 μm). Though not all combinations passed, these values are dependent on the chosen thresholding. In addition, the pupil image is oversampled with 60 pixels diameter compared to the projection onto the MEMS deformable mirror, which is 43 $\times$ 43 actuators.

(iii) RMS common distortion:

$$CD = \sqrt{\frac{\sum_{i=2}^{N}(|\frac{S_i}{S1} - \frac{avg(A_i,B_i,C_i,D_i)}{avg(A1,B1,C1,D1)}|^2)}{N-1}} \tag{3}$$

where $S_i/S1$ is the normalised radius of entrance pupil $\frac{avg(A_i,B_i,C_i,D_i)}{avg(A1,B1,C1,D1)}$ is the normalised pupil image radius (average of the four pupils) and N is the total number of points used around the pupil. The RMS common distortion requirement was < 4 μm and was measured to be much smaller at 0.5 μm.

3.3 Relative Rotation

The relative rotation was also measured by using the resolution card at the pupil plane and moving light into each quadrant. As indicated by Figure 6, with the dashed white line across a line of the resolution card, the orientation of each pupil is the same.

3.4 Linearity

Since there were no means to apply a tip/tilt at the pupil plane, the aberration was applied using FSM1 (i.e. the modulation stage) to measure a preliminary linearity curve, as shown in Figure 7, without modulation. Though this is not the final linearity result, the PWFS produces the characteristic linearity shape. This will be redone on the GPI 2.0 bench, utilising the deformable mirror to apply low-order modes, with and without modulation.

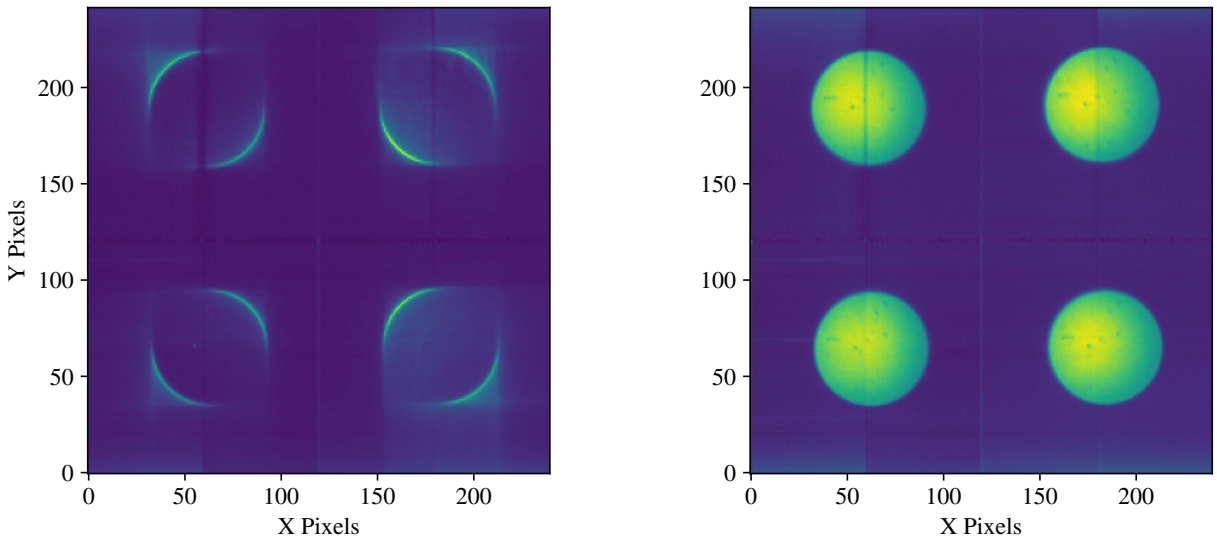

Figure 3. Pupil images with a non-modulated (left) and modulated (right) beam.

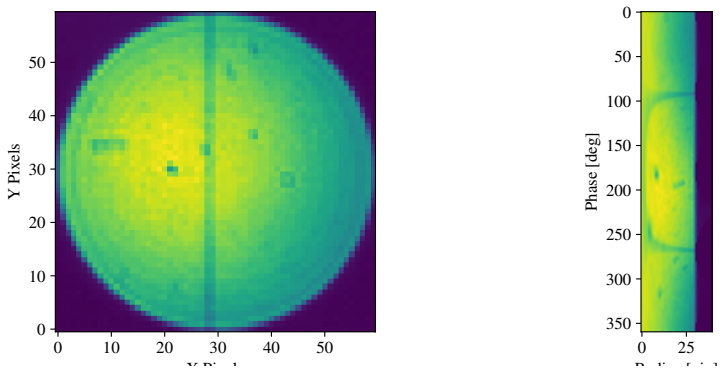

Figure 4. E ulate the radius and distortion.

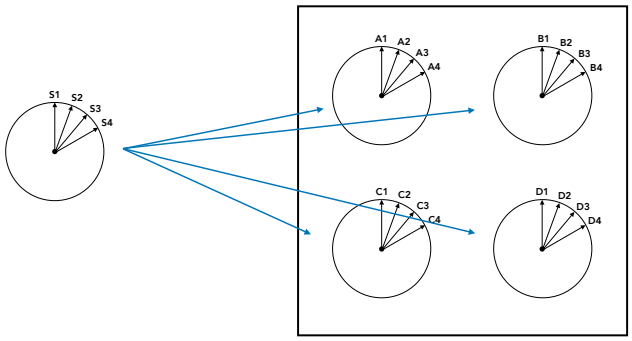

Figure 5. Pupil distortion calculation.

4. CONCLUSION

We have presented the pre-integrated characterisation of the GPI 2.0 PWFS. The results show that we are within the requirements for throughput, pupil diameter, pupil separation and RMS common distortion. The difference in the expected pupil differential distortion is marginal. In May 2024 the PWFS was integrated into GPI 2.0. In July 2024 we will align the PWFS relative to the rest of the GPI instrument. To achieve this, partial RTC integration must take place to control the stages and mirrors located before the PWFS, to receive the beam at its default position. Following the alignment, the tests presented in this paper will be redone and calibration will begin. The calibration will include closing the loop on static aberrations and validating linearity and dynamic range against simulations. GPI 2.0 is expected to complete integration and ship to the Gemini North Telescope in 2024B/2025A with general science observations in 2025B.[9]

ACKNOWLEDGMENTS

GPI 2.0 is funded in part by the Heising-Simons Foundation through grant 2019-1582. The GPI project has been supported by Gemini Observatory, which is operated by AURA, Inc., under a cooperative agreement with the NSF on behalf of the Gemini partnership: the NSF (USA), the National Research Council (Canada), CONICYT (Chile), the Australian Research Council (Australia), MCTI (Brazil) and MINCYT (Argentina). Portions of this work were performed under the auspices of the U.S. Department of Energy by Lawrence Livermore National Laboratory under Contract DE-AC52-07NA27344.

REFERENCES

[1] Nielsen, E. L., De Rosa, R. J., Macintosh, B., Wang, J. J., Ruffio, J.-B., Chiang, E., Marley, M. S., Saumon, D., Savransky, D., Ammons, S. M., Bailey, V. P., Barman, T., Blain, C., Bulger, J., Burrows, A., Chilcote,

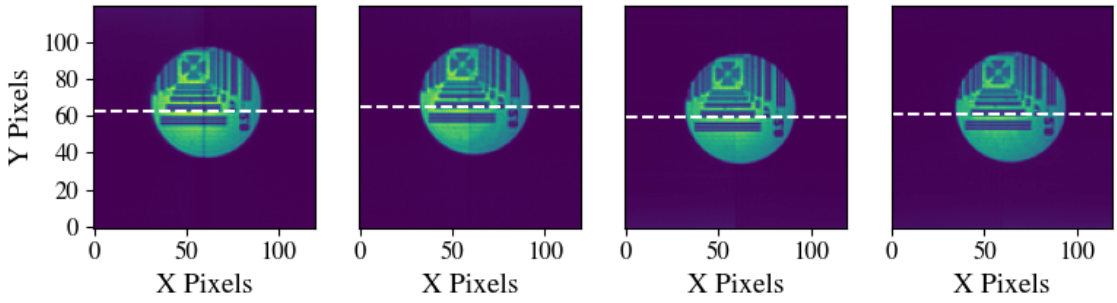

Figure 6. The four pupils (left to right: A, B, C, D) with a resolution card at the pupil plane. The white dashed line shows no relative rotation of the pupil.

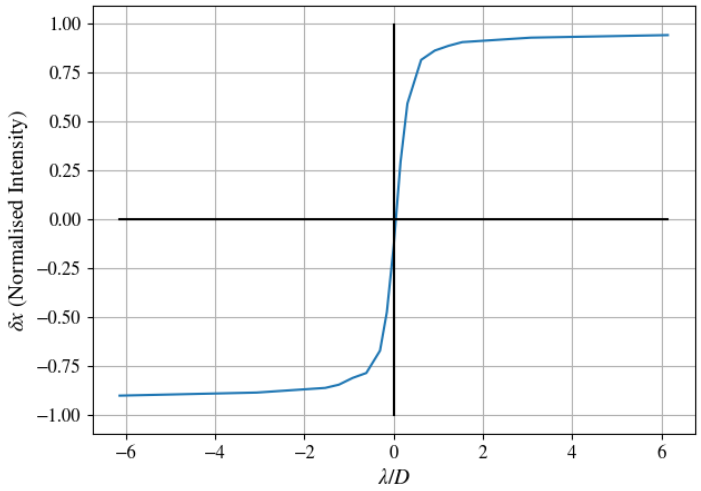

Figure 7. Linearity of the non-modulated PWFS.

J., Cotten, T., Czekala, I., Doyon, R., Duchêne, G., Esposito, T. M., Fabrycky, D., Fitzgerald, M. P., Follette, K. B., Fortney, J. J., Gerard, B. L., Goodsell, S. J., Graham, J. R., Greenbaum, A. Z., Hibon, P., Hinkley, S., Hirsch, L. A., Hom, J., Hung, L.-W., Dawson, R. I., Ingraham, P., Kalas, P., Konopacky, Q., Larkin, J. E., Lee, E. J., Lin, J. W., Maire, J., Marchis, F., Marois, C., Metchev, S., Millar-Blanchaer, M. A., Morzinski, K. M., Oppenheimer, R., Palmer, D., Patience, J., Perrin, M., Poyneer, L., Pueyo, L., Rafikov, R. R., Rajan, A., Rameau, J., Rantakyrö, F. T., Ren, B., Schneider, A. C., Sivaramakrishnan, A., Song, I., Soummer, R., Tallis, M., Thomas, S., Ward-Duong, K., and Wolff, S., "The Gemini Planet Imager Exoplanet Survey: Giant Planet and Brown Dwarf Demographics from 10 to 100 au," **158**, 13 (July 2019).

[2] Chilcote, J., Konopacky, Q., Rosa, R. J. D., Hamper, R., Macintosh, B., Marois, C., Perrin, M. D., Savransky, D., Soummer, R., Véran, J.-P., Agapito, G., Aleman, A., Ammons, S. M., Bonaglia, M., Boucher, M.-A., Curliss, M., Dunn, J., Esposito, S., Filion, G., Fitzsimmons, J., Kain, I., Kerley, D., Landry, J.-T., Lardiere, O., Lemoine-Busserolle, M., Li, D., Limbach, M. A., Madurowicz, A., Maire, J., N'Diaye, M., Nielsen, E. L., Poyneer, L., Pueyo, L., Summey, K., and Thomas, C., "GPI 2.0: upgrading the Gemini Planet Imager," in [*Ground-based and Airborne Instrumentation for Astronomy VIII*], Evans, C. J., Bryant, J. J., and Motohara, K., eds., **11447**, 394 – 407, International Society for Optics and Photonics, SPIE (2020).

[3] Peng, D. H., Chilcote, J., Konopacky, Q. M., Hamper, R., Sands, B., Bruke, J., Engstrom, M., Karaszewksi, A., Boyle, R., Limbach, M. A., Perera, S., Do Ó, C. R., Nguyen, J., Macintosh, B., Fitzsimmons, J., Marois, C., Rantakyrö, F. T., Aleman, A., Maire, J., Rosa, R. J., Por, E., Savransky, D., Meiji, N., Perrin, M., Soummer, R., Pueyo, L., Nickson, B., and Spalding, E., "Testing and performance of IFS upgrades for GPI

2.0," in [*Optics+Photonics*], *Society of Photo-Optical Instrumentation Engineers (SPIE) Conference Series*, 12680–71 (2023).

[4] Kerley, D., Smith, M. J., Véran, J.-P., Dunn, J. S., and Gharavi, N., "Herzberg extensible adaptive real-time toolkit (heart) software architecture," 6th International Conference on Adaptive Optics for Extremely Large Telescopes, AO4ELT 2019 (2019).

[5] Crane, J., Herriot, G., Andersen, D., Atwood, J., Byrnes, P., Densmore, A., Dunn, J., Fitzsimmons, J., Hardy, T., Hoff, B., Jackson, K., Kerley, D., Lardière, O., Smith, M., Stocks, J., Véran, J.-P., Boyer, C., Wang, L., Trancho, G., and Trubey, M., "NFIRAOS adaptive optics for the Thirty Meter Telescope," in [*Adaptive Optics Systems VI*], Close, L. M., Schreiber, L., and Schmidt, D., eds., **10703**, 1094 – 1106, International Society for Optics and Photonics, SPIE (2018).

[6] Fitzsimmons, J., Agapito, G., Bonaglia, M., Boucher, M.-A., Chilcote, J., Dunn, J., Esposito, S., Filion, G., Kerley, D., Konopacky, Q., Landry, J.-T., Lardiere, O., Macintosh, B., Madurowicz, A., Maire, J., Marois, C., Poyneer, L., Savransky, D., and Veran, J.-P., "GPI 2.0: design of the pyramid wave front sensor upgrade for GPI," in [*Adaptive Optics Systems VII*], Schreiber, L., Schmidt, D., and Vernet, E., eds., **11448**, 1299 – 1311, International Society for Optics and Photonics, SPIE (2020).

[7] Do-Ó, C. R., Perera, S., Maire, J., Nguyen, J. S., Chambouleyron, V., Konopacky, Q. M., Chilcote, J., Fitzsimmons, J., Hamper, R., Kerley, D., Macintosh, B., Marois, C., Rantakyrö, F., Savranksy, D., Veran, J.-P., Agapito, G., Ammons, S. M., Bonaglia, M., Boucher, M.-A., Dunn, J., Esposito, S., Filion, G., Landry, J. T., Lardiere, O., Li, D., Madurowicz, A., Peng, D., Poyneer, L., and Spalding, E., "GPI 2.0: exploring the impact of different readout modes on the wavefront sensor's EMCCD," **13097**, International Society for Optics and Photonics, SPIE (2024).

[8] Perera, S., Maire, J., Ó, C. R. D., Nguyen, J. S., Levinstein, D. M., Konopacky, Q. M., Chilcote, J., Fitzsimmons, J., Hamper, R., Kerley, D., Macintosh, B., Marois, C., Rantakyrö, F., Savransky, D., Veran, J.-P., Agapito, G., Ammons, S. M., Bonaglia, M., Boucher, M.-A., Dunn, J., Esposito, S., Filion, G., Landry, J. T., Lardiere, O., Li, D., Dillon, D., Madurowicz, A., Peng, D., Poyneer, L., and Spalding, E., "GPI 2.0: pyramid wavefront sensor status," in [*Adaptive Optics Systems VIII*], Schreiber, L., Schmidt, D., and Vernet, E., eds., **12185**, 121854C, International Society for Optics and Photonics, SPIE (2022).

[9] Chilcote, J., "GPI 2.0: upgrade status of the Gemini Planet Imager," **13096**, International Society for Optics and Photonics, SPIE (2024).